

See discussions, stats, and author profiles for this publication at: <https://www.researchgate.net/publication/320175038>

# Oxygen-assisted preparation of mechanoluminescent ZnS:Mn for dynamic pressure mapping

Article in *Nano Research* · October 2017

DOI: 10.1007/s12274-017-1813-y

CITATIONS

0

READS

39

6 authors, including:



**Xiandi Wang**

Beijing Institute of Nanoenergy and Nanosyste...

16 PUBLICATIONS 261 CITATIONS

[SEE PROFILE](#)



**Rui Ling**

University of Science and Technology Beijing

1 PUBLICATION 0 CITATIONS

[SEE PROFILE](#)



**Miaoling Que**

Beijing Institute of Nanoenergy and Nanosyste...

8 PUBLICATIONS 72 CITATIONS

[SEE PROFILE](#)



**Caofeng Pan**

Chinese Academy of Sciences

125 PUBLICATIONS 4,021 CITATIONS

[SEE PROFILE](#)

Some of the authors of this publication are also working on these related projects:



ZnO/Si LED and piezo-phototronic effect [View project](#)



nanomaterial [View project](#)

All content following this page was uploaded by [Xiandi Wang](#) on 13 October 2017.

The user has requested enhancement of the downloaded file.

# Oxygen-assisted preparation of mechanoluminescent ZnS:Mn for dynamic pressure mapping

Xiandi Wang<sup>1,2</sup>, Rui Ling<sup>1,3</sup>, Yufei Zhang<sup>1,4</sup>, Miaoling Que<sup>1,2</sup>, Yiyao Peng<sup>1,2</sup>, and Caofeng Pan<sup>1,2</sup> (✉)

<sup>1</sup> Beijing Institute of Nanoenergy and Nanosystems, Chinese Academy of Sciences, Beijing 100083, China

<sup>2</sup> CAS Center for Excellence in Nanoscience, National Center for Nanoscience and Technology (NCNST), Beijing 100190, China

<sup>3</sup> School of Materials Science and Engineering, University of Science and Technology Beijing, Beijing 100083, China

<sup>4</sup> Key Laboratory of Aerospace Materials and Performance (Ministry of Education), School of Materials Science and Engineering, Beihang University, Beijing 100191, China

Received: 15 June 2017

Revised: 11 August 2017

Accepted: 20 August 2017

© Tsinghua University Press  
and Springer-Verlag GmbH  
Germany 2017

## KEYWORDS

oxygen assistance,  
piezo-photonic effect,  
pressure mapping,  
ZnS:Mn

## ABSTRACT

Mechanoluminescent materials that convert mechanical stimuli to light emission have attracted extensive attention for potential applications in human–machine interactions. Here, we report a simple and available novel approach for the oxygen-assisted preparation of ZnS:Mn particles by solid-state reaction at atmospheric pressure without the formation of the corresponding oxides. The existence of O<sub>2</sub> has a positive impact on the formation of S vacancies in wurtzite-phase ZnS, leading to the introduction of Mn<sup>2+</sup> ion luminescent centers and shallow donor levels, which can improve the electron–hole recombination rate. The O<sub>2</sub> ratio and Mn<sup>2+</sup> ion doping concentration have significant effects on the luminous efficiency, which is optimal at 1%–20% and 1 at.%–2 at.% respectively. In addition, a device based on the piezo-photonic effect with excellent pressure sensitivity of 0.032 MPa<sup>-1</sup> was fabricated, which can map the two-dimensional pressure distribution ranging from 2.2 to 40.6 MPa *in situ*. This device can be applied to real-time pressure mapping, smart sensor networks, high-level security systems, human-machine interfaces, and artificial skins.

## 1 Introduction

Mechanoluminescent materials, which can convert mechanical stress to light emission, have attracted extensive attention because of their advantages in zero-powered stress visualization [1–4]. They are promising candidates for applications in tactile imaging, human-machine interfaces, self-powered systems,

and information security [5–9]. Recently, elastic mechanoluminescence (EML)—one form of mechanoluminescence (ML) [10]—has attracted interest worldwide due to nondestructive analysis [11] that can be detected in inorganic crystalline materials including fluorides, chalcogenides, phosphates, oxysulfides, titanates, and aluminates [12–19]. SrAl<sub>2</sub>O<sub>4</sub> and ZnS stand out among these ML compounds due to their

Address correspondence to cspan@binn.cas.cn

high luminous efficiencies and the regulation of color and chemical stability by introducing various dopant ions [20–22]. However, the typical preparation technique for ZnS:Mn is based on a vacuum solid-state reaction, which results in the large loss of elements and imprecise control of the doping amount owing to the saturated vapor pressure.

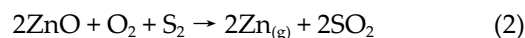
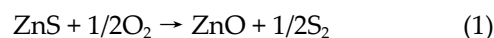
The physical mechanism of the ML process in ZnS:Mn can be explained by the piezo-phonic effect [23–27], which is a two-way coupling effect between piezoelectricity and photo-excitation properties. Upon imposition of strain, a piezoelectric potential is generated within wurtzite ZnS from the introduction of piezoelectric polarization charges [28, 29]. The potential tilts the band structure, resulting in the detrapping of electrons in the conduction band. The energy is transferred to excite Mn<sup>2+</sup> ions by the non-radioactive recombination of detrapped electrons and holes. Then, excited Mn<sup>2+</sup> ions go back to the ground state (<sup>6</sup>A<sub>1</sub> (<sup>6</sup>S) → <sup>4</sup>T<sub>1</sub> (<sup>4</sup>G)), giving off orange emission. During the entire ML process, the strain-induced piezoelectric potential plays a significant role in tuning and controlling the photo-excitation process. According to this mechanism, two-dimensional pressure distribution can be observed by analyzing the visible light emitted from ZnS:Mn [30–32].

Here, we demonstrate a simple and novel method for the synthesis of ZnS:Mn particles via solid-state reaction at normal pressure with the help of oxygen. This can effectively reduce the loss of products and thus control the doping amount. Meanwhile, it offers a direct method to understand the effects of S vacancies induced by O<sub>2</sub>, which can generate additional luminescence centers of Mn<sup>2+</sup> ions and introduce shallow donor levels to accelerate electron–hole recombination. The O<sub>2</sub> ratio and Mn<sup>2+</sup> ion doping concentration—whose optimal values are 1%–20% and 1 at.%–2 at.%, respectively—play essential roles in the photoluminescence (PL) and ML processes. Moreover, a device with outstanding pressure sensitivity of 0.032 MPa<sup>-1</sup> in the range 2.2–40.6 MPa was fabricated for dynamic pressure mapping to convert mechanical stimuli to optical signals without applying external power. The visible display of pressure distribution demonstrated by the device illustrates potential application for intelligent electronic skins, human–

machine interfaces, tactile imaging, and information safety [33–36].

## 2 Results and discussion

ZnS:Mn particles were prepared via high-temperature solid-state reactions at normal pressure in atmospheres with different ratios of Ar and O<sub>2</sub>. Figure 1(a) gives a schematic illustration of the reaction equipment. Briefly, ZnS and MnCO<sub>3</sub> powders were mixed well in a certain ratio (e.g. 1 at.% Mn<sup>2+</sup> ions) and then compacted into an alumina boat. Unlike the vacuum environment used in previous works [8, 37], we synthesized the samples at atmospheric pressure with the assistance of O<sub>2</sub>. The original air was taken out using a pump and a mixture of Ar and O<sub>2</sub> with constant velocity was immediately added into the quartz tube. The valve was opened after the pressure reached 10<sup>5</sup> Pa to keep the pressure constant during the sintering process. The role of O<sub>2</sub> during the reaction process can be interpreted as follows



Obviously, free Zn atoms can be formed in the presence of oxygen and a small amount of sulfur leaves the lattice in the form of sulfur dioxide. According to chemical thermodynamics theory [38], the change of free energy,  $\Delta G$ , is given by  $\Delta G = \Delta H - T\Delta S$  at constant temperature and pressure, where  $\Delta H$  and  $\Delta S$  are the changes of enthalpy and entropy, respectively,  $T$  is the sintering temperature. Reaction proceeds spontaneously if  $\Delta G < 0$ . Hence, it is found that reaction (1) might occur spontaneously at any temperature while the sintering temperature should be higher than 526 °C for reaction (2). In this work, the samples were sintered at 1,100 °C for 3 h, which provided a favorable condition for the formation of free zinc atoms. Subsequently, these free zinc atoms would enter the positions of Zn<sup>2+</sup> ions in the ZnS lattice by physical–chemistry processes like absorption and diffusion. Thus, a complex defect structure with sulfur vacancies and interstitial zinc atoms is achieved to maintain electrical neutrality in the crystal. Additionally, these defects are the key condition for the formation of Mn

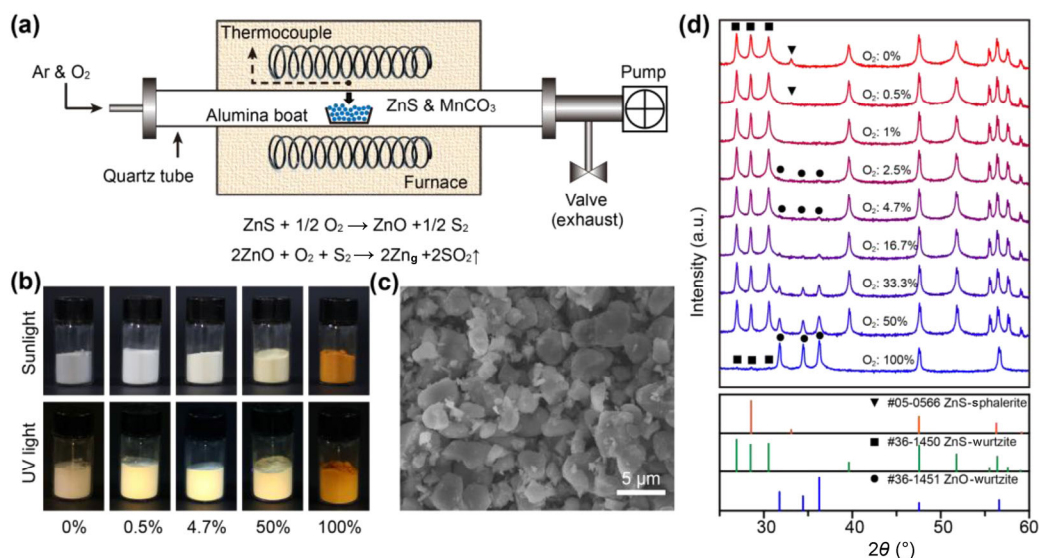


**Figure 1** Synthesis and characterization of ZnS:Mn particles. (a) Schematic of the reaction system. (b) Photographs of ZnS:Mn samples (prepared in atmospheres with different  $O_2$  ratios) under sunlight and UV light. (c) SEM image of the ZnS:Mn particles doped with 1 at.%  $Mn^{2+}$  ions sintered at  $1,100\text{ }^\circ\text{C}$  for 3 h when the  $O_2$  ratio is 2.5%. (d) XRD patterns of samples (logarithmic  $Y$ -axis) synthesized at different  $O_2$  ratios.

centers, which can introduce MnO into the crystal. Therefore, it is inferred that the presence of  $O_2$  promotes the formation of crystal defects, resulting in the effective generation of activator centers.

The morphologies and crystal structures of the as-synthesized samples were investigated. Figure 1(b) shows the powders sintered in atmospheres with different  $O_2$  contents. It was found that the colors of the samples start from grey then turn to white and finally yellow (under sunlight) with the increase of  $O_2$  ratio. Furthermore, the samples emitted yellow light when activated by ultraviolet (UV) light. Compared with the first four samples, the last one, however, showed no evident changes. Hence, we presume that the particles synthesized with low- $O_2$  atmospheres have superior fluorescence properties when activated by UV light, while the samples prepared under high- $O_2$  atmospheres change the original compositions and thus have no apparent luminescence. Upon further grinding and screening, the samples prepared at different  $O_2$  ratios had similar morphologies. The scanning electron microscopy (SEM) image of a typical sample at 2.5%  $O_2$  ratio is presented in Fig. 1(c), demonstrating that the average size of particles was about  $5\text{ }\mu\text{m}$ . X-ray powder diffraction (XRD) was carried out to further confirm the crystal structures of

the as-synthesized samples, shown in Fig. 1(d). It is clear that only wurtzite-phase ZnS and a small quantity of sphalerite-phase ZnS existed in the samples when the  $O_2$  ratio was  $\leq 1\%$ . No other diffraction peaks of oxide and manganese compounds were obtained. This result indicates that the presence of  $O_2$  can accelerate the phase transformation of ZnS without introducing other corresponding oxides. However, the volume ratio of wurtzite-phase ZnO increased with  $O_2$  content when the  $O_2$  ratio was more than 2.5%. Only a small amount of wurtzite-phase ZnS was observed when it increased to 100%, i.e., the sample changed significantly from ZnS to ZnO, stopping the orange light emission under UV light (370 nm). As discussed above, it can be deduced that the samples start getting oxidized at 2.5%  $O_2$ , but still mainly consist of ZnS despite the formation of small amounts of ZnO when the  $O_2$  ratio is less than 50 at.%, which also demonstrates fine fluorescence properties.

The elementary compositions of the products were further characterized by energy dispersive spectrometry (EDS). Figures 2(a)–2(c) shows the elemental distributions of Zn, S, Mn, and O in a couple of typical samples sintered in atmospheres with different  $O_2$  ratios. In samples with  $O_2$  ratios from 1% to 50%, the major components were Zn and S, and Mn element

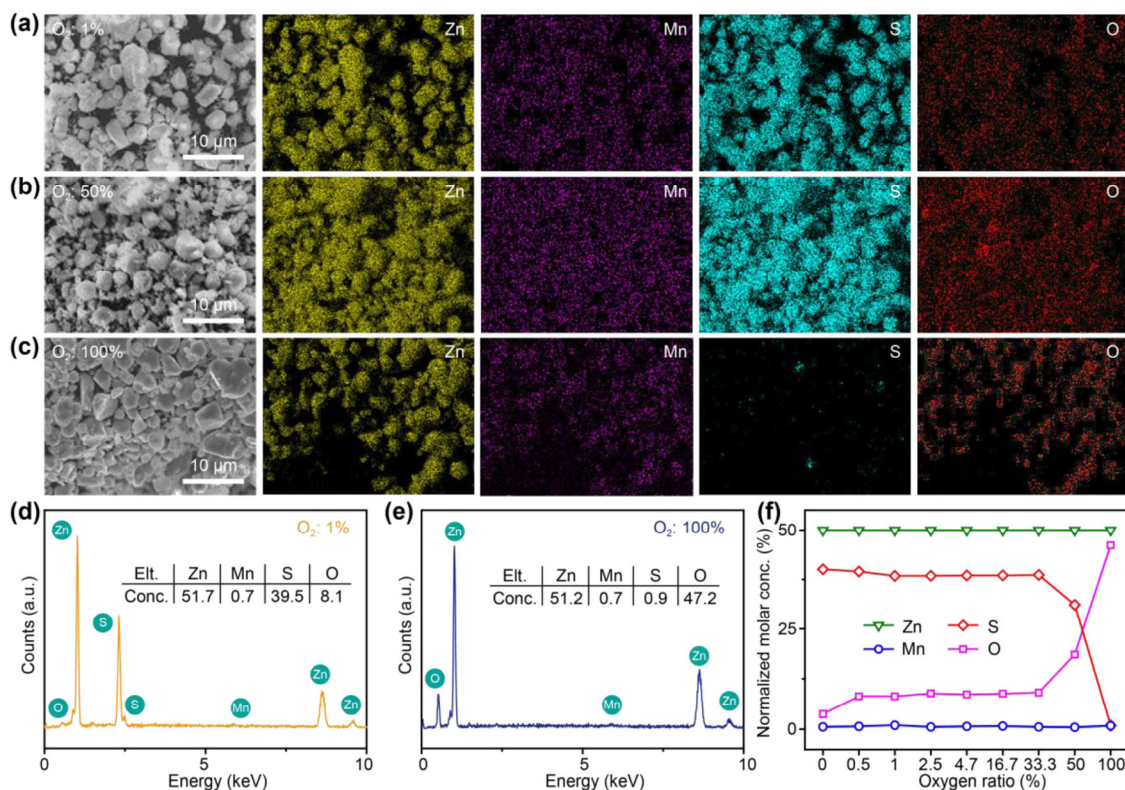


**Figure 2** Elemental analysis of ZnS:Mn particles. (a)–(c) EDS images: corresponding elemental maps of Zn, Mn, S, and O when the O<sub>2</sub> ratios are 1%, 50%, and 100%, respectively. (d) and (e) Energy dispersive X-ray spectra of the samples. (f) Changes of each element in the products as a function of the O<sub>2</sub> ratio.

was evenly distributed in the scanned area without agglomeration, illustrating the presence of ZnS:Mn. However, when the O<sub>2</sub> ratio reached 100%, O became the main constituent of the sample (instead of S). Detailed elemental information of these samples is semi-quantitatively described in Figs. 2(d) and 2(e). Normalizing by the zinc molar concentration, we obtained changes of each element with the O<sub>2</sub> ratio, as shown in Fig. 2(f). It was found that the atomic ratios of O and S remained nearly constant when O<sub>2</sub> ratio varied from 0 to 33.3%, which is consistent with the XRD results discussed above. Meanwhile, the concentration of O suddenly increased and that of S decreased significantly when the samples were sintered in a complete oxygen atmosphere. Additionally, the molar concentration of Mn (about 0.7 at.% by calculation) was close to the original doping concentration (1 at.%), which remained constant. Crucially, the proportion of positive ions was greater than that of negative ions in any sample, which provides direct evidence of the existence of sulfur vacancies.

The effects of sulfur vacancies on the band structure and electric properties of ZnS were illustrated by first-principles calculations based on density functional theory (DFT). Figures 3(a) and 3(b) show the energy band structure, and the partial and total electronic densities of states (PDOS and DOS) of a pure ZnS supercell system in which the Fermi energy level is 0 eV. It is obvious that the bottom of the conduction band and the top of the valence band are located at the same *k*-point (G), indicating that it is a direct band gap semiconductor. Inevitably, the band gap calculated using local density functional theory is always lower than the experimental value due to the neglect of excited states. Nevertheless, the results can still be suitable for qualitative analysis after corrections using the scissors approximation. In this work, the band gap of pure ZnS was estimated to be 2.158 eV, which is significantly smaller than the experimental value (3.77 eV), and thus a scissors correction of 1.61 eV was employed. Moreover, the conduction band (2 to 5 eV) is mainly composed of the Zn 4s and S 3p states

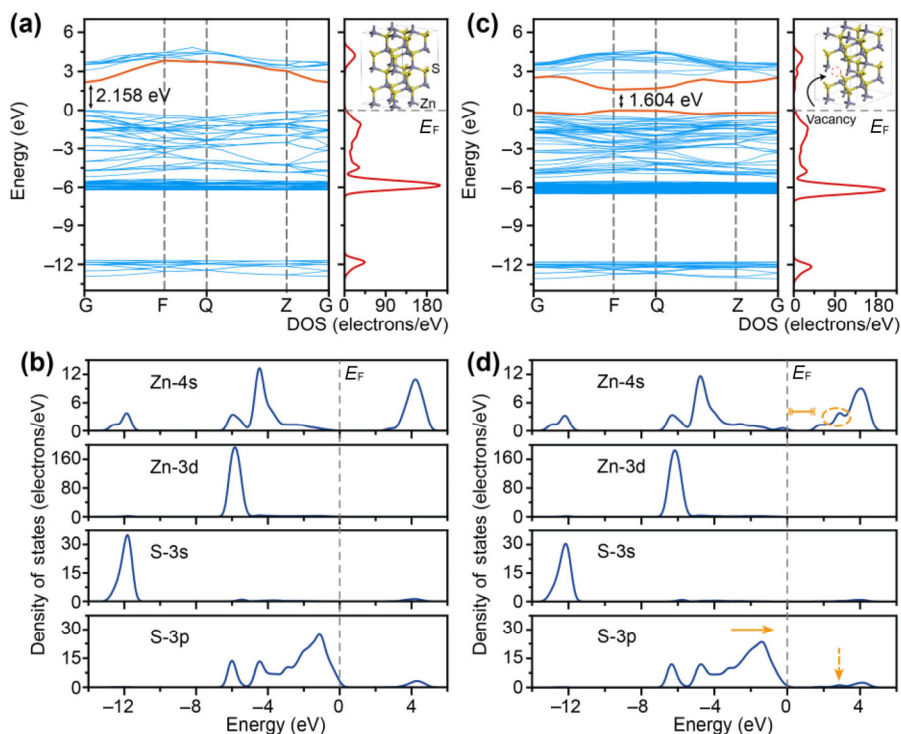


**Figure 3** Band structure and electric property of ZnS. (a) Band structure of intact ZnS and its total density of states. (b) Partial density of states of intact ZnS. (c) Band structure of ZnS with S vacancies and its total density of states. (d) Partial density of states of ZnS with S vacancies.

while the valence band consists of two parts in which the upper valence band ( $-5.3$  to  $0$  eV) is chiefly dominated by S 3p states and the lower valence band ( $-6.4$  to  $-5.3$  eV) is dominated by Zn 3d states. Compared with the pure ZnS model, the energy band structures and DOS display remarkable variation due to the presence of sulfur vacancies, as shown in Figs. 2(c) and 2(d). The bottom of the conduction band moved to the low-energy region and the top of the valence band moved toward the high-energy region. That is, the band gap between impurity-induced bands became smaller ( $1.604$  eV), which resulted from the change in DOS of Zn 4s states when S vacancies were introduced. As discussed above, we can infer that the presence of S vacancies helps introduce shallow donor levels, resulting in band-gap reduction, which in turn assists in the process of electron-hole recombination and increases the luminous efficiency.

The PL properties of products with different  $\text{Mn}^{2+}$  ions doping concentrations sintered in different atmospheres were carefully investigated using a continuous laser ( $325$  nm). Figure 4(a) shows the

corresponding PL spectra of samples with 1 at.%  $\text{Mn}^{2+}$  ions synthesized in atmospheres with different  $\text{O}_2$  ratios. These spectra had a common peak near  $585$  nm in the emission range  $500$ – $700$  nm, corresponding to orange light. The spectral intensity integrated over  $500$ – $700$  nm as a function of  $\text{O}_2$  ratio is presented in Fig. 4(b). The emission intensity increased with the  $\text{O}_2$  ratio initially and dropped when the  $\text{O}_2$  ratio exceeded 33.3%. Actually, during the solid-state reaction, higher  $\text{O}_2$  partial pressure in the sintering atmosphere enhanced the concentration of S vacancies, which promoted the formation of  $\text{Mn}^{2+}$  ion luminescent centers and introduced shallow donor levels. Hence, PL property will be significantly improved with increasing  $\text{O}_2$  ratio in the beginning. However, increasing numbers of ZnO particles were formed when the  $\text{O}_2$  content increased further, which no longer could be activated to emit orange light, leading to gradually weakening luminescent intensity. In addition, the  $\text{Mn}^{2+}$  ion doping concentration also had a primary effect on optical performance, as shown in Figs. 4(c) and 4(d). Similar spectra were obtained from samples

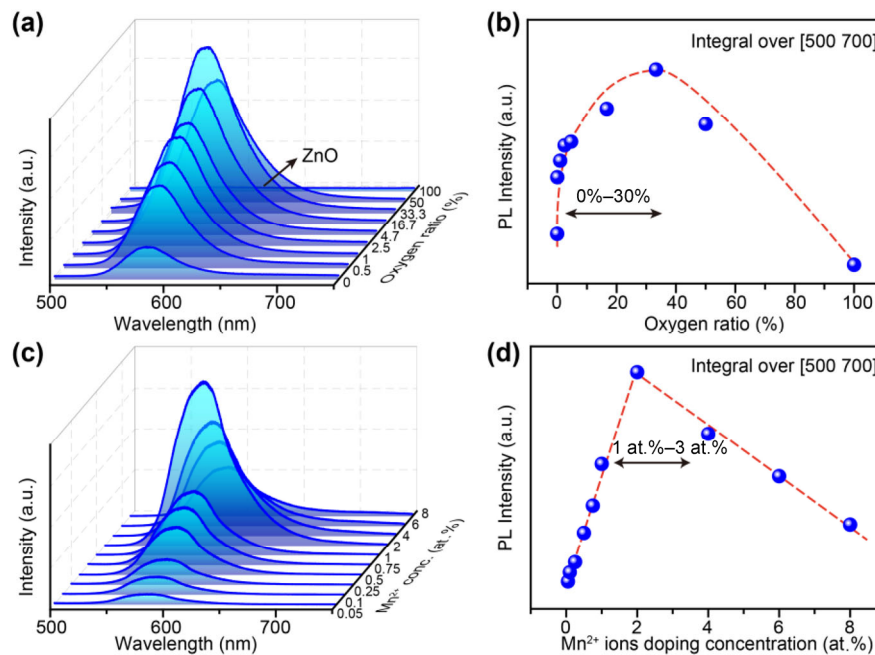


**Figure 4** Characterization of PL performance. (a) PL spectra of samples sintered in atmospheres with different O<sub>2</sub> ratios. (b) Integrated intensity over 500–700 nm of these spectra versus O<sub>2</sub> ratio. (c) PL spectra of the samples with different Mn<sup>2+</sup> ion doping concentrations. (d) Integrated PL intensity as a function of Mn<sup>2+</sup> ions doping concentration.

with different doping concentrations; the integral PL intensity increased at first and then declined. We infer that more luminescence centers can be formed by increasing the Mn<sup>2+</sup> ion doping concentration, resulting in the linear and remarkable enhancement of PL intensity. However, the decrease of luminescence intensity results from the existence of excessive Mn<sup>2+</sup> ions and Mn-Mn pairs when the doping concentration exceeded 2% [8]. Thus, the concentrations of both S vacancies and Mn<sup>2+</sup> ions are key factors contributing to the PL performances of the products. The optimal O<sub>2</sub> ratio is 0–30%, and Mn<sup>2+</sup> ion doping concentration is 1 at.%–3 at.%.

ML performances of the samples were subsequently characterized by applying different pressures on as-synthesized devices. The device preparation method and the test equipment are mentioned in previous works [7, 8]. A device with 0.5 g ZnS:Mn particles packaged in 0.1 mm thick polyethylene terephthalate (PET) was employed to obtain the ML performance. Figure 5(a) demonstrates the ML spectra of the device under different load forces, illustrating that the emission intensity increased with applied force. The wavelength of the luminescence center was around

585 nm, which is consistent with the PL data. In fact, the ML of ZnS:Mn particles is based on the piezophotonic effect, which is a coupling effect between piezoelectricity and photo-excitation [24, 39–41]. Briefly, piezoelectric polarization charges are induced in ZnS due to its non-central symmetry after application of pressure, leading to tilting of the band structure and non-radioactive recombination between electrons and holes. By transferring energy, the Mn<sup>2+</sup> ions are excited and then fall to the ground state by emitting orange light (<sup>4</sup>T<sub>1</sub>→<sup>6</sup>A<sub>1</sub>). It is obvious that the piezoelectric potential plays a valuable role in the ML process. Additionally, the pressure sensitivity of the product, defined as the slope of ML intensity versus applied pressure, was estimated to be about 0.032 MPa<sup>-1</sup> in the range 2.2–40.6 MPa after standard calibration, as shown in Fig. 5(b). Finally, we explored the influences of the concentrations of S vacancies and Mn<sup>2+</sup> ions on ML properties. Similar to PL characterization, both factors had their optimal parameters: 1%–20% and 1 at.%–2 at.% for the O<sub>2</sub> ratio and the Mn<sup>2+</sup> ion doping concentration, respectively, as shown in Figs. 5(c) and 5(d).

Notably, the as-synthesized ZnS:Mn particles had

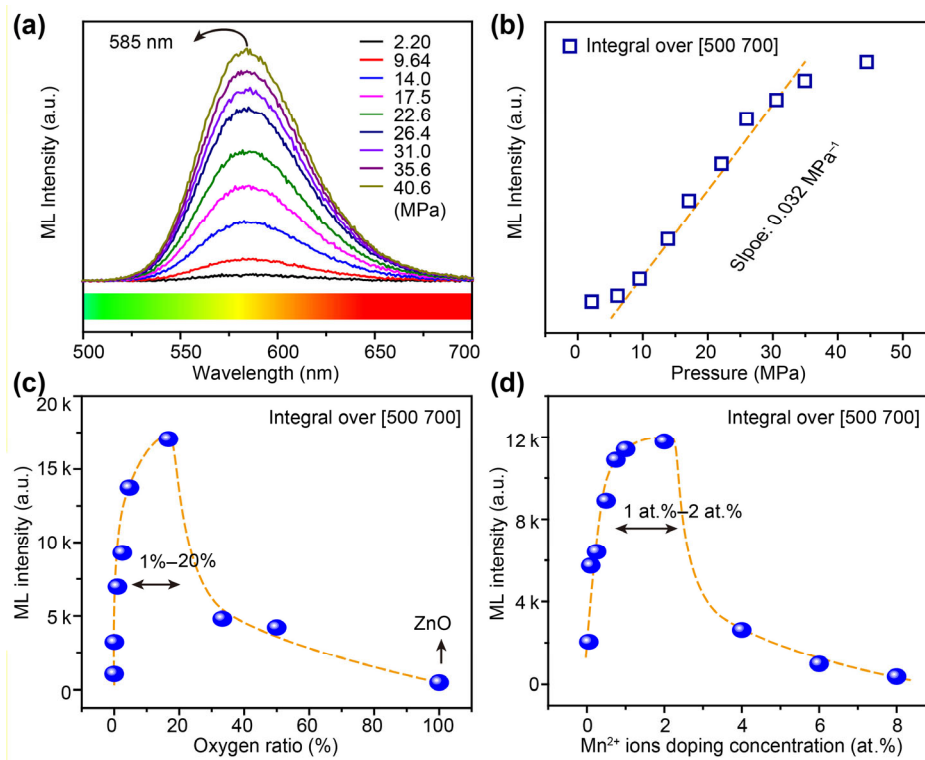


**Figure 5** Characterization of the ML performance. (a) ML spectra of the products under different applied forces. (b) Integral ML intensity over 500–700 nm as a function of pressure. (c) Influence of the concentration of S vacancies on the ML property. All samples were prepared via a normal pressure solid-state reaction by sintering at 1,100 °C for 3 h with 1 at.% Mn<sup>2+</sup> ions. (d) Influence of the Mn<sup>2+</sup> ion doping concentration on the ML property. All samples were sintered at atmospheric pressure with 2.5% O<sub>2</sub> ratio.

high sensitivity in the high-pressure regime (> 1 MPa), which can be used in intelligent signatures, artificial electronic skins, and human-machine interactions. Here, we demonstrated the application of the device to dynamic stress imaging. An image acquisition and processing system controlled by a computer with self-developed software was employed to complete the recording and processing of optical signals in parallel [7, 8]. Figure 6(a) presents a schematic illustration of the operation of the device. Orange light with different intensities will be emitted from the device when the applied pressure changes, which will be detected by the image processing system. Then the visual pressure distribution is obtained in real-time by signal processing techniques. A detailed illustration of the dynamic pressure mapping process is shown in Fig. 6(b), which exhibits the capture of handwritten letters “A”, “B”, and “C” at different pressures. Two-dimensional distribution of ML intensity was first obtained by the measurement system, as shown at the

bottom of Fig. 6(b). By extracting and analyzing the gray scale of the captured image, three-dimensional distribution of the light intensity was subsequently observed. Hence, the pressure profile can be calculated from the linear relationship between the ML intensity or gray value and the applied stress, as shown in the top of Fig. 6(b). In this manner, the device can convert mechanical stress to an optical signal, which is then precisely monitored and reveals pressure information through the measuring system.

### 3 Conclusions

We demonstrated a novel method for the preparation of ZnS:Mn particles via solid-state reaction with the assistance of oxygen as a promising way to exactly control the doping amount. The presence of O<sub>2</sub> accelerates the formation of S vacancies, which introduces additional Mn<sup>2+</sup> ion luminescence centers and introduces shallow donor levels to reduce the

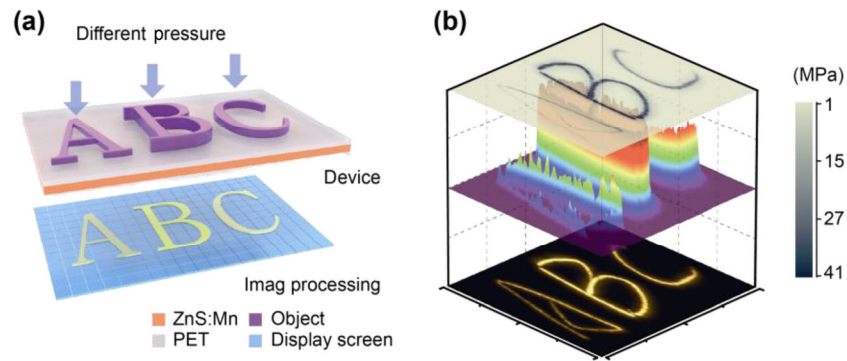


**Figure 6** Performance of the device for intelligent signature. (a) Schematic illustration of the pressure mapping process. (b) Detecting the ML intensity and recording the pressure distribution.

band gap. It was noted that no other corresponding oxides were formed when the sintering atmosphere contained low levels of oxygen, according to the XRD and EDS analyses. The influences of the concentrations of S vacancies and  $\text{Mn}^{2+}$  ions on the PL and ML properties were explored, indicating that the optimal  $\text{O}_2$  ratio and  $\text{Mn}^{2+}$  ion doping concentration are 1%–20% and 1 at.%–2 at.%, respectively. Additionally, a device with excellent pressure sensitivity of  $0.032 \text{ MPa}^{-1}$  in the range 2.2–40.6 MPa was fabricated for the secure collection of electronic signatures that can convert mechanical stress into an optical signal and exhibit the pressure distribution upon data processing. We predict that the synthetic method presented can be widely used in the fabrication of other mechanoluminescent materials that will possess extensive application in information safety, human–machine interfaces, and intelligent electronic skins.

## 4 Experimental

### 4.1 Synthesis and characterization of ZnS:Mn particles

ZnS:Mn particles were synthesized by a high temperature solid-state reaction at atmospheric pressure. ZnS (99.99%, Aladdin) and  $\text{MnCO}_3$  (99.95%, Aladdin) powders were used as raw material. The two powders were mixed in a certain proportion by wet grinding. The mixture was compacted into an alumina boat and loaded in a furnace and sintered in atmospheres with different  $\text{O}_2$  ratios at  $1,100 \text{ }^\circ\text{C}$  for 3 h. Finally, the products were ground and screened to characterize

their crystal structures. X-ray diffraction with  $\text{Cu-K}\alpha$  radiation in the  $\theta$ - $2\theta$  scanning mode was employed to study the crystallization of the powders (X'Pert3 Powder). Field-emission scanning electron microscopy (Hitachi, SU8020) was utilized to observe the morphologies of the samples and energy dispersive X-ray spectroscopy (IXRF, SDD2830-300D) was carried out to analyze the elemental components.

### 4.2 Model and calculation method

Crystal structure data of wurtzite ZnS with the space group P63/mc ( $a = b = 3.8195 \text{ \AA}$ ,  $c = 6.2552 \text{ \AA}$ ,  $\alpha = \beta = 90^\circ$ ,  $\gamma = 120^\circ$ ) was used to optimize the geometry and calculate electronic properties. A series of  $2 \times 2 \times 2$  ZnS supercells with and without sulfur vacancies were constructed to study the effect of sulfur vacancies on band structure, as depicted in the inset of Figs. 3(a) and 3(b). All calculations were performed using the Cambridge Serial Total Energy Package (CASTEP) in Material Studios 8.0, which contains first-principles calculations based on density function theory (DFT). The ultra-soft pseudo-potential was employed to substitute the electron-ion interactions and Perdew–Burke–Ernzerhof functional (PBE) under the generalized gradient approximation (GGA) was adopted to describe the exchange and correlation potentials of the electronic–electronic interaction. In our calculation, the energy cut-off was set to 350 eV and the Brillouin zones were built by a  $4 \times 4 \times 2$   $k$ -point mesh.

### 4.3 PL and ML measurements

Photoluminescence spectra were collected using

LabRAM HR Evolution. A home-made measurement system including the acquisitions of optical signal and stress analysis was used to obtain the ML spectra. In this system, a spectrometer (Ocean Optics QE65pro) was used to collect the emitted light and a pressure sensor (Nano17 ATI) was employed to detect the stress on the device.

## Acknowledgements

The authors are thankful for support from National Natural Science Foundation of China (Nos. 51622205, 61675027, 61405040, 51432005, 61505010, and 51502018), National Key R & D project from Minister of Science and Technology, China (No. 2016YFA0202703), National Postdoctoral Program for Innovative Talents (No. BX201600040), China Postdoctoral Science Foundation Funded Project (No. 2016M600976) and the “Thousand Talents” program of China for pioneering researchers and innovative teams.

## References

- [1] Camara, C. G.; Escobar, J. V.; Hird, J. R.; Putterman, S. J. Correlation between nanosecond X-ray flashes and stick-slip friction in peeling tape. *Nature* **2008**, *455*, 1089–1092.
- [2] Eddingsaas, N. C.; Suslick, K. S. Mechanoluminescence: Light from sonication of crystal slurries. *Nature* **2006**, *444*, 163.
- [3] Jeong, S. M.; Song, S.; Lee, S. K.; Ha, N. Y. Color manipulation of mechanoluminescence from stress-activated composite films. *Adv. Mater.* **2013**, *25*, 6194–6200.
- [4] Jeong, S. M.; Song, S.; Kim, H. Simultaneous dual-channel blue/green emission from electro-mechanically powered elastomeric zinc sulphide composite. *Nano Energy* **2016**, *21*, 154–161.
- [5] Jeong, S. M.; Song, S.; Lee, S. K.; Choi, B. Mechanically driven light-generator with high durability. *Appl. Phys. Lett.* **2013**, *102*, 051110.
- [6] Li, F.; Wang, X. D.; Xia, Z. G.; Pan, C. F.; Liu, Q. L. Photoluminescence tuning in stretchable pdms film grafted doped core/multishell quantum dots for anticounterfeiting. *Adv. Funct. Mater.* **2017**, *27*, 1700051.
- [7] Wang, X. D.; Que, M. L.; Chen, M. X.; Han, X.; Li, X. Y.; Pan, C. F.; Wang, Z. L. Full dynamic-range pressure sensor matrix based on optical and electrical dual-mode sensing. *Adv. Mater.* **2017**, *29*, 1605817.
- [8] Wang, X. D.; Zhang, H. L.; Yu, R. M.; Dong, L.; Peng, D. F.; Zhang, A. H.; Zhang, Y.; Liu, H.; Pan, C. F.; Wang, Z. L. Dynamic pressure mapping of personalized handwriting by a flexible sensor matrix based on the mechanoluminescence process. *Adv. Mater.* **2015**, *27*, 2324–2331.
- [9] Wang, X. D.; Dong, L.; Zhang, H. L.; Yu, R. M.; Pan, C. F.; Wang, Z. L. Recent progress in electronic skin. *Adv. Sci.* **2015**, *2*, 1500169.
- [10] Chandra, B. P.; Xu, C. N.; Yamada, H.; Zheng, X. G. Luminescence induced by elastic deformation of ZnS:Mn nanoparticles. *J. Lumin.* **2010**, *130*, 442–450.
- [11] Peng, D. F.; Chen, B.; Wang, F. Recent advances in doped mechanoluminescent phosphors. *ChemPlusChem* **2015**, *80*, 1209–1215.
- [12] Tu, D.; Xu, C. N.; Yoshida, A.; Fujihala, M.; Hirotsu, J.; Zheng, X. G. LiNbO<sub>3</sub>:Pr<sup>3+</sup>: A multipiezo material with simultaneous piezoelectricity and sensitive piezoluminescence. *Adv. Mater.* **2017**, *29*, 1606914.
- [13] Wang, X.; Xu, C. N.; Yamada, H.; Nishikubo, K.; Zheng, X. G. Electro-mechano-optical conversions in Pr<sup>3+</sup>-doped BaTiO<sub>3</sub>-CaTiO<sub>3</sub> ceramics. *Adv. Mater.* **2005**, *17*, 1254–1258.
- [14] Cho, S.; Kang, S.; Pandya, A.; Shanker, R.; Khan, Z.; Lee, Y.; Park, J.; Craig, S. L.; Ko, H. Large-area cross-aligned silver nanowire electrodes for flexible, transparent, and force-sensitive mechanochromic touch screens. *ACS Nano* **2017**, *11*, 4346–4357.
- [15] Kim, G.; Cho, S.; Chang, K.; Kim, W. S.; Kang, H.; Ryu, S. P.; Myoung, J.; Park, J.; Park, C.; Shim, W. Spatially pressure-mapped thermochromic interactive sensor. *Adv. Mater.* **2017**, *29*, 1606120.
- [16] Hirai, Y.; Nakanishi, T.; Kitagawa, Y.; Fushimi, K.; Seki, T.; Ito, H.; Hasegawa, Y. Triboluminescence of lanthanide coordination polymers with face-to-face arranged substituents. *Angew. Chem.* **2017**, *129*, 7277–7281.
- [17] Gan, J. Y.; Kang, M. G.; Meeker, M. A.; Khodaparast, G. A.; Bodnar, R. J.; Mahaney, J. E.; Maurya, D.; Priya, S. Enhanced piezoluminescence in non-stoichiometric Zn<sub>s</sub>:Cu microparticles based light emitting elastomers. *J. Mater. Chem. C* **2017**, *5*, 5387–5394.
- [18] Li, L. J.; Wong, K. L.; Li, P. F.; Peng, M. Y. Mechanoluminescence properties of Mn<sup>2+</sup>-doped BaZnOS phosphor. *J. Mater. Chem. C* **2016**, *4*, 8166–8170.
- [19] Yang, Y. B.; Yang, X. D.; Tan, Y. N.; Yuan, Q. Recent progress in flexible and wearable bio-electronics based on nanomaterials. *Nano Res.* **2017**, *10*, 1560–1583.
- [20] Xu, C. N.; Watanabe, T.; Akiyama, M.; Zheng, X. G. Direct view of stress distribution in solid by mechanoluminescence. *Appl. Phys. Lett.* **1999**, *74*, 2414–2416.
- [21] Fang, H. J.; Wang, X. D.; Li, Q.; Peng, D. F.; Yan, Q. F.;

- Pan, C. F. A stretchable nanogenerator with electric/light dual-mode energy conversion. *Adv. Energy Mater.* **2016**, *6*, 1600829.
- [22] Xu, C. N.; Yamada, H.; Wang, X. S.; Zheng, X. G. Strong elasticoluminescence from monoclinic-structure  $\text{SrAl}_2\text{O}_4$ . *Appl. Phys. Lett.* **2004**, *84*, 3040–3042.
- [23] Wang, Z. L. Towards self-powered nanosystems: From nanogenerators to nanopiezotronics. *Adv. Funct. Mater.* **2008**, *18*, 3553–3567.
- [24] Wang, Z. L. Piezopotential gated nanowire devices: Piezotronics and piezo-phototronics. *Nano Today* **2010**, *5*, 540–552.
- [25] Yu, R. M.; Dong, L.; Pan, C. F.; Niu, S. M.; Liu, H. F.; Liu, W.; Chua, S.; Chi, D. Z.; Wang, Z. L. Piezotronic effect on the transport properties of GaN nanobelts for active flexible electronics. *Adv. Mater.* **2012**, *24*, 3532–3537.
- [26] Pan, C. F.; Dong, L.; Zhu, G.; Niu, S. M.; Yu, R. M.; Yang, Q.; Liu, Y.; Wang, Z. L. High-resolution electroluminescent imaging of pressure distribution using a piezoelectric nanowire LED array. *Nat. Photonics* **2013**, *7*, 752–758.
- [27] Wu, W. Z.; Wen, X. N.; Wang, Z. L. Taxel-addressable matrix of vertical-nanowire piezotronic transistors for active and adaptive tactile imaging. *Science* **2013**, *340*, 952–957.
- [28] Chen, L.; Wong, M. C.; Bai, G. X.; Jie, W. J.; Hao, J. H. White and green light emissions of flexible polymer composites under electric field and multiple strains. *Nano Energy* **2015**, *14*, 372–381.
- [29] Huang, L. B.; Xu, W.; Bai, G. X.; Wong, M. C.; Yang, Z. B.; Hao, J. H. Wind energy and blue energy harvesting based on magnetic-assisted noncontact triboelectric nanogenerator. *Nano Energy* **2016**, *30*, 36–42.
- [30] Hu, G. F.; Guo, W. X.; Yu, R. M.; Yang, X. N.; Zhou, R. R.; Pan, C. F.; Wang, Z. L. Enhanced performances of flexible ZnO/perovskite solar cells by piezo-phototronic effect. *Nano Energy* **2016**, *23*, 27–33.
- [31] Wang, C. F.; Bao, R. R.; Zhao, K.; Zhang, T. P.; Dong, L.; Pan, C. F. Enhanced emission intensity of vertical aligned flexible ZnO nanowire/p-polymer hybridized led array by piezo-phototronic effect. *Nano Energy* **2015**, *14*, 364–371.
- [32] Wen, X. N.; Wu, W. Z.; Pan, C. F.; Hu, Y. F.; Yang, Q.; Wang, Z. L. Development and progress in piezotronics. *Nano Energy* **2015**, *14*, 276–295.
- [33] Hu, G. F.; Zhou, R. R.; Yu, R. M.; Dong, L.; Pan, C. F.; Wang, Z. L. Piezotronic effect enhanced schottky-contact ZnO micro/nanowire humidity sensors. *Nano Res.* **2014**, *7*, 1083–1091.
- [34] Qiu, J. C.; Zhao, K.; Li, L. L.; Yu, X.; Guo, W. B.; Wang, S.; Zhang, X. D.; Pan, C. F.; Wang, Z. L.; Liu, H. A titanium dioxide nanorod array as a high-affinity nano-bio interface of a microfluidic device for efficient capture of circulating tumor cells. *Nano Res.* **2017**, *10*, 776–784.
- [35] Zhang, T. P.; Liang, R. R.; Dong, L.; Wang, J.; Xu, J.; Pan, C. F. Wavelength-tunable infrared light emitting diode based on ordered ZnO nanowire/ $\text{Si}_{1-x}\text{Ge}_x$  alloy heterojunction. *Nano Res.* **2015**, *8*, 2676–2685.
- [36] Wang, X. D.; Zhang, H. L.; Dong, L.; Han, X.; Du, W. M.; Zhai, J. Y.; Pan, C. F.; Wang, Z. L. Self-powered high-resolution and pressure-sensitive triboelectric sensor matrix for real-time tactile mapping. *Adv. Mater.* **2016**, *28*, 2896–2903.
- [37] Xu, C. N.; Watanabe, T.; Akiyama, M.; Zheng, X. G. Artificial skin to sense mechanical stress by visible light emission. *Appl. Phys. Lett.* **1999**, *74*, 1236–1238.
- [38] Kollman, P. Free energy calculations: Applications to chemical and biochemical phenomena. *Chem. Rev.* **1993**, *93*, 2395–2417.
- [39] Chen, Y.; Zhang, Y.; Karnaushenko, D.; Chen, L.; Hao, J. H.; Ding, F.; Schmidt, O. G. Addressable and color-tunable piezophotonic light-emitting stripes. *Adv. Mater.* **2017**, *29*, 1605165.
- [40] Wong, M. C.; Chen, L.; Tsang, M. K.; Zhang, Y.; Hao, J. H. Magnetic-induced luminescence from flexible composite laminates by coupling magnetic field to piezophotonic effect. *Adv. Mater.* **2015**, *27*, 4488–4495.
- [41] Zhang, Y.; Gao, G. Y.; Chan, H. L. W.; Dai, J. Y.; Wang, Y.; Hao, J. H. Piezo-phototronic effect-induced dual-mode light and ultrasound emissions from  $\text{ZnS:Mn/PMN-Pt}$  thin-film structures. *Adv. Mater.* **2012**, *24*, 1729–1735.